Spatial resolution and efficiency of prototype sensors for the LHCb VELO Upgrade

E. Buchanan,[a,c,*] **K. Akiba,**[b] **M. van Beuzekom,**[b] **P. Collins,**[c] **E. Dall'Occo,**[b,d] **T. Evans,**[c,e] **V. Franco Lima,**[f] **R. Geertsema,**[b] **P. Kopciewicz,**[g] **E. Price,**[a] **B. Rachwal,**[g] **S. Richards,**[a] **D. Saunders,**[a] **H. Schindler,**[c] **T. Szumlak,**[g] **P. Tsopelas,**[b,h] **J. Velthuis**[a] **and M.R.J. Williams**[i]

[a]*University of Bristol, Beacon House,*
Queens Road, BS8 1QU, Bristol, U.K.

[b]*Nikhef,*
Science Park 105, 1098 XG Amsterdam, the Netherlands

[c]*CERN,*
1211 Geneve, Switzerland

[d]*TU Dortmund,*
Otto-Hahn-Straße 4, 44227 Dortmund, Germany

[e]*University of Oxford, Particle Physics Department,*
Denys Wilkinson Bldg., Keble Road, Oxford OX1 3RH, U.K.

[f]*Oliver Lodge Laboratory, University of Liverpool,*
Liverpool, L69 7ZE, U.K.

[g]*AGH University of Science and Technology, Faculty of Physics and Applied Computer Science,*
Kraków, Poland

[h]*Spectricon, Science and Technology Park of Crete,*
Heraklion, Greece

[i]*School of Physics and Astronomy, University of Edinburgh,*
Edinburgh, U.K.

E-mail: emma.buchanan@cern.ch

ABSTRACT: A comprehensive study of the spatial resolution and detection efficiency of sensor prototypes developed for the LHCb VELO upgrade is presented. Data samples were collected at the CERN SPS H8 beam line using a hadron mixture of protons and pions with momenta of approximately 180 GeV/c. The sensor performance was characterised using both irradiated and non-irradiated sensors. Irradiated samples were subjected to a maximum fluence of 8×10^{15} 1 MeV n_{eq} cm^{-2}, of both protons and neutrons. The spatial resolution is measured comparing the detected hits to the position as predicted by tracks reconstructed by the Timepix3 telescope. The resolution is presented for different applied bias voltages and track angles, sensor thickness and implant size.

*Corresponding author.

Contents

1   Introduction

The LHCb experiment is upgrading its VErtex LOcator (VELO) detector during Long Shutdown 2 of the LHC to allow the experiment to operate at an instantaneous luminosity of $\mathcal{L} = 2 \times 10^{33}$ cm^{-2} s^{-1}, five times higher than previous runs [1]. The VELO requires very precise tracking and fast pattern recognition in order to reconstruct collisions and decay vertices in real time as the first step of the LHCb trigger decision. The VELO upgrade will replace the original detector's silicon strips with hybrid pixel detectors, which consist of planar silicon sensors bump-bonded to VeloPix [2] readout ASICs (Application Specific Integrated Circuits).

The region of the detector closest to the collision point will be exposed to a total integrated fluence of $\phi = 8 \times 10^{15}$ 1 MeV n$_{eq}$ cm^{-2} [1]. To maintain an excellent tracking and vertexing

performance through its lifetime, the detector must remain fully efficient (> 99%) up to the maximum fluence levels.

This paper presents the spatial resolution and the hit efficiency of several different prototype devices designed for the VELO upgrade, before and after being irradiated up to 8×10^{15} 1 MeV n_{eq} cm^{-2} with both uniform and non-uniform fluence profiles.

The sensor prototypes are planar silicon pixel sensors, with square pixels of 55 μm pitch, bonded to Timepix3 ASICs [3], which can measure simultaneously the particles Time-Of-Arrival (TOA) and Time-Over-Threshold (TOT). The TOA is measured with 1.56 ns TDC bin width and the TOT is proportional to the charge collected by each pixel, and calibrated as described in refs. [4, 5]. The threshold is set to 1000 e$^-$ to ensure negligible noise. The sensor performance has been evaluated using a charged hadron beam. Tracks are reconstructed using the Timepix3 Telescope [4].

This paper is organised as follows. Firstly, the experimental setup is described in section 2. The main results are then presented in sections 3, 4 and 5, describing the cluster distributions, efficiency and spatial resolution, respectively. Finally, the applicability of the prototype sensors regarding the running conditions in the LHCb experiment is discussed in section 6.

2 Prototype sensors and experimental setup

2.1 Prototype devices

The prototype sensors were produced by two different manufacturers, Hamamatsu Photonics K. K. (HPK)[1] and Micron Semiconductor Ltd.[2] The prototypes have different design features in terms of pixel implant size, sensor thickness, bulk type and the pixel-to-edge (PTE) distance (see table 1). The HPK sensors have been produced with n$^+$-type implants separated by p$^+$-stop implants on a 200 ± 20 μm thick float-zone p-doped silicon substrate (resistivity of 3-8 kΩ cm). The back of the sensor consists of a thin p$^+$-doped layer and is fully metallised. Two different guard ring designs with PTE of 450 and 600 μm. The pixel implants are either 35 or 39 μm squares with rounded corners. The Micron prototypes have been produced with 36 μm wide n$^+$-type implants with rounded corners and p$^+$-spray isolation. Two different types of substrates have been used: 200 μm p-type (> 5 kΩ cm) and 150 μm n-type (> 1.5 kΩ cm). The latter is double sided processed with guard rings on the backside of the sensor partially implanted underneath the edge pixels. The back of these sensors consist of a thin p$^+$-doped layer and the back for the p-type substrate is fully metallised, while for the n-type substrate the back is metallised in a grid structure. For these sensors there are two PTE variants with corresponding distances of 250 μm and 450 μm. The n$^+$-p-p$^+$ (n$^+$-n-p$^+$) sensors are from now on referred to as n-on-p (n-on-n) sensors. The details of individual assemblies and their identification numbers, which are used in the following sections, can be found in appendix A.

The depletion voltages were measured to be around ~120 V for HPK devices and ~40 V for both types of Micron devices [6, 7]. A subset of devices were uniformly irradiated with neutrons at JSI [8], up to 8×10^{15} 1 MeV n_{eq} cm^{-2}, referred to as full fluence. Another group of devices were non-uniformly irradiated at the IRRAD facility at CERN [9], which provides a 24 GeV proton beam that has approximately a two-dimensional Gaussian distribution. This is used to emulate the

---

[1]Hamamatsu Photonics K. K., 325-6, Sunayama-cho, Naka-ku, Hamamatsu City, Shizuoka, 430-8587, Japan.
[2]Micron Semiconductor Ltd, 1 Royal Buildings, Marlborough Road, Lancing BN158UN, United Kingdom.

Table 1. Prototype assemblies.

Vendor	Type	Thickness	PTE	Implant width
HPK	n-on-p	$200\,\mu m$	$450, 600\,\mu m$	$35, 39\,\mu m$
Micron	n-on-p	$200\,\mu m$	$450\,\mu m$	$36\,\mu m$
Micron	n-on-n	$150\,\mu m$	$250, 450\,\mu m$	$36\,\mu m$

variation in the fluence anticipated across the inner VELO sensors at the end of their lifetime. The reconstructed fluence profile [10] is shown in appendix B.

2.2 The Timepix3 telescope and track reconstruction

An extensive test beam programme has been carried out at the SPS H8 beamline at CERN [11] to characterise the sensors. The beam is composed of a mixture of charged hadrons (∼67% protons, ∼30% pions) at 180 GeV/c. The Timepix3 telescope [4] is a high rate, data-driven beam telescope, composed of two arms of four planes each. Each plane is equipped with a $300\,\mu m$ p-on-n silicon sensor that is bump bonded to a Timepix3 ASIC, which is operated with a $1000\,e^-$ threshold. The centre of the telescope is reserved for the Device Under Test (DUT). The DUT area is equipped with remotely controlled motion stages able to translate in x and y directions, with z as the beam axis and rotate about the y axis. A vacuum box can also be installed on the central stage to facilitate testing of irradiated devices at high voltage. The cooling block connected to the ASIC can be cooled down to temperatures of $-35°C$, which keeps the sensors below $-20°C$. The temperature of the cold box is measured with a Pt100, which is converted to the corresponding sensor temperature using a calibration curve. This calibration curve is determined before the testbeam in a dedicated lab setup. In this setup a Pt100 was glued to the sensor itself and another Pt100 was glued to the cold box in order to measure the sensor temperature for different cold box temperatures. The pointing resolution at the DUT position is about $1.6\,\mu m$, enabling intrapixel studies of the DUT. The typical temporal resolution on a track using only the Timepix3 timestamps is about 350 ps [12].

Tracks are only reconstructed if hits are found in all eight telescope planes within 20 ns. The 20 ns time window is sufficient to reject most events with two tracks overlapping nearby in space and in time. The maximum cluster size on each plane is set to 10 and the track fit χ^2 is required to be below 10. A DUT cluster is associated to a track if its position is within a $100\,\mu m$ and 35 ns from the track intercept reconstructed by the telescope.

2.3 Spatial resolution measurement

The orthogonal, x (or y), position of a traversing particle through the sensor is reconstructed using the Centre of Gravity (CoG) method as:

$$x = \frac{\sum_{\text{cluster}} S_i \cdot x_i}{\sum_{\text{cluster}} S_i}, \tag{2.1}$$

where x_i is the coordinate of the ith pixel in the cluster and S_i is the signal measured in the corresponding pixel. The resolution of this interpolation depends on the signal-to-noise ratio of the sensor and on the digitisation precision of the front-end, as well as on the threshold value set. For

the purposes of this paper the resolution on the charge measurement performed by the Timepix3 front-end gives a negligible contribution to the CoG uncertainty.

The figure of merit adopted to compare the spatial performance of the prototypes is the resolution given by the width of the residual distribution, where residual is defined as the difference between the track intercept estimated from the trajectory fit, provided by the telescope (section 2.2) and the cluster position reconstructed using the sensor. The width of the residual distribution, σ_{residual}, incorporates not only the intrinsic resolution of the sensor σ_{sensor} but also the telescope pointing resolution $\sigma_{\text{telescope}}$:

$$\sigma_{\text{residual}}^2 = \sigma_{\text{sensor}}^2 + \sigma_{\text{telescope}}^2. \tag{2.2}$$

The intrinsic spatial resolution of the sensor is therefore obtained by subtracting in quadrature from the measured width of the residual distribution the telescope resolution.

The residual distribution for a Micron n-on-p sensor is shown in figure 1. The distribution has a distinctive double peak feature due to fact that the fraction of charge shared between two pixels is not linearly related to the distance between the intercept and the mid point of the pixels [13]. In this analysis the non-linear effect is not corrected. The spatial resolution is quantified as the RMS of the residual distribution considering only a range of ±3 times the raw Root Mean Square (RMS) of the entire distribution. This quantity is referred to as the *truncated RMS*.
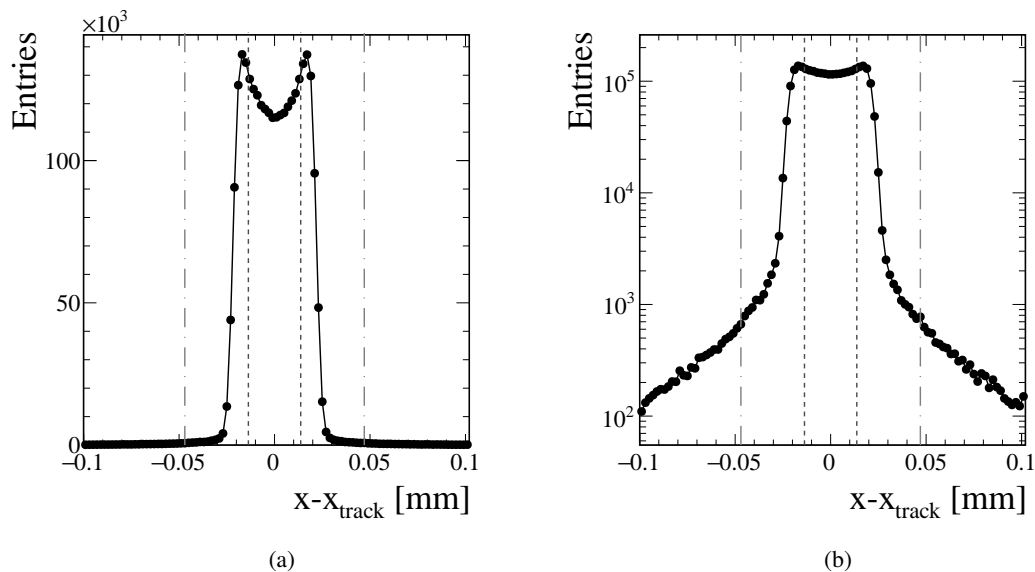

Figure 1. Example residual distribution for a HPK n-on-p sensor (S6), placed perpendicular to the beam and operated near the full depletion voltage (a), logarithmic scale (b). The outer dashed lines indicate ±3×RMS and the inner dashed lines indicate the *truncated RMS*.

For charged particles traversing at an angle, the path of the particle through the sensor bulk is greater than that of a perpendicular track. This results in an increase in the liberated charge and an increased probability that particles will cross multiple pixels. Neglecting the threshold and diffusion effects and considering only two pixels, the angle that leads to the optimal spatial resolution (θ_{opt})

is given in terms of the pixel pitch and detector thickness by:

$$\theta_{\mathrm{opt}} = \tan^{-1}\left(\frac{\text{pitch}}{\text{thickness}}\right). \tag{2.3}$$

From this, θ_{opt} is 15° for 200 μm thick sensors and 20° for 150 μm thick sensors.

2.4 Cluster finding efficiency

The efficiency is defined as the ratio of the number of clusters matched to a track and the total number of reconstructed tracks. The error on the efficiency is calculated as the error from the binomial distribution. The telescope allows the efficiency to be measured as a function of intrapixel position.

3 Analysis of cluster sizes and charge sharing

The position with which a track traverses within a pixel influences charge sharing between pixels. Figure 2 shows the track intercept locations within the pixel, known as intrapixel track position, for size 1, 2, 3 & 4 for a Micron n-on-p sensor placed perpendicular to the beam and operated near the full depletion voltage. Size 1 clusters are mainly from tracks passing through the centre of the pixel. Size two clusters originate from tracks hitting the pixel edges, while tracks at the corners result in cluster sizes of 3 and 4 pixels. In general cluster size 3 and 4 only account for ~5% of all clusters for perpendicular tracks.

3.1 Bias voltage

Higher electric fields increase the drift velocity and subsequently reduce the lateral diffusion due to a shorter charge collection time [14]. This effect is studied by measuring the cluster size distribution as a function of the applied bias voltage for sensors placed perpendicular to the beam, shown in figures 3 (a) and (b). For the 200 μm n-on-p devices and voltages below full depletion (40 V for Micron sensors and 120 V for HPK), the diffusion between pixels is largest but the majority of clusters remain of size 1. As the sensor is not fully depleted the collected charge is small, and hence the charge shared with neighbouring pixels does not reach the threshold. Increasing the bias up to the full depletion voltage improves the charge collection efficiency [7], which in turn increases the probability that the shared charge will cross the threshold, leading to higher fractions of size 2 clusters, and consequently decreasing the fraction of size 1. The minimum in the fraction of cluster size 1 and hence the maximum in the fraction of size 2, corresponds to the full depletion voltage. The peak of size 2 clusters is overall higher and appears at a lower voltage for the Micron n-on-p sensors because the depletion voltage is lower compared to the HPK n-on-p sensors and hence the electric fields are weaker, leading to more diffusion. Above full depletion voltage, the electric field strength continues to increase, but now reduces the charge sharing due to shorter drift times and therefore lower lateral diffusion.

For the Micron n-on-n sensors the trend differs because the junction develops from the backplane of the sensor instead of the pixel implants. Below full depletion (40 V), the field is weak in the vicinity of the implants and thus the charge diffuses further, which enhances charge sharing and hence the fraction of size 2 clusters. The weak field region is always narrow enough, about 20 μm [6], that the charge will diffuse towards the implants and thus be collected. As the applied bias voltage increases, the field strengthens, the diffusion and charge sharing is suppressed and
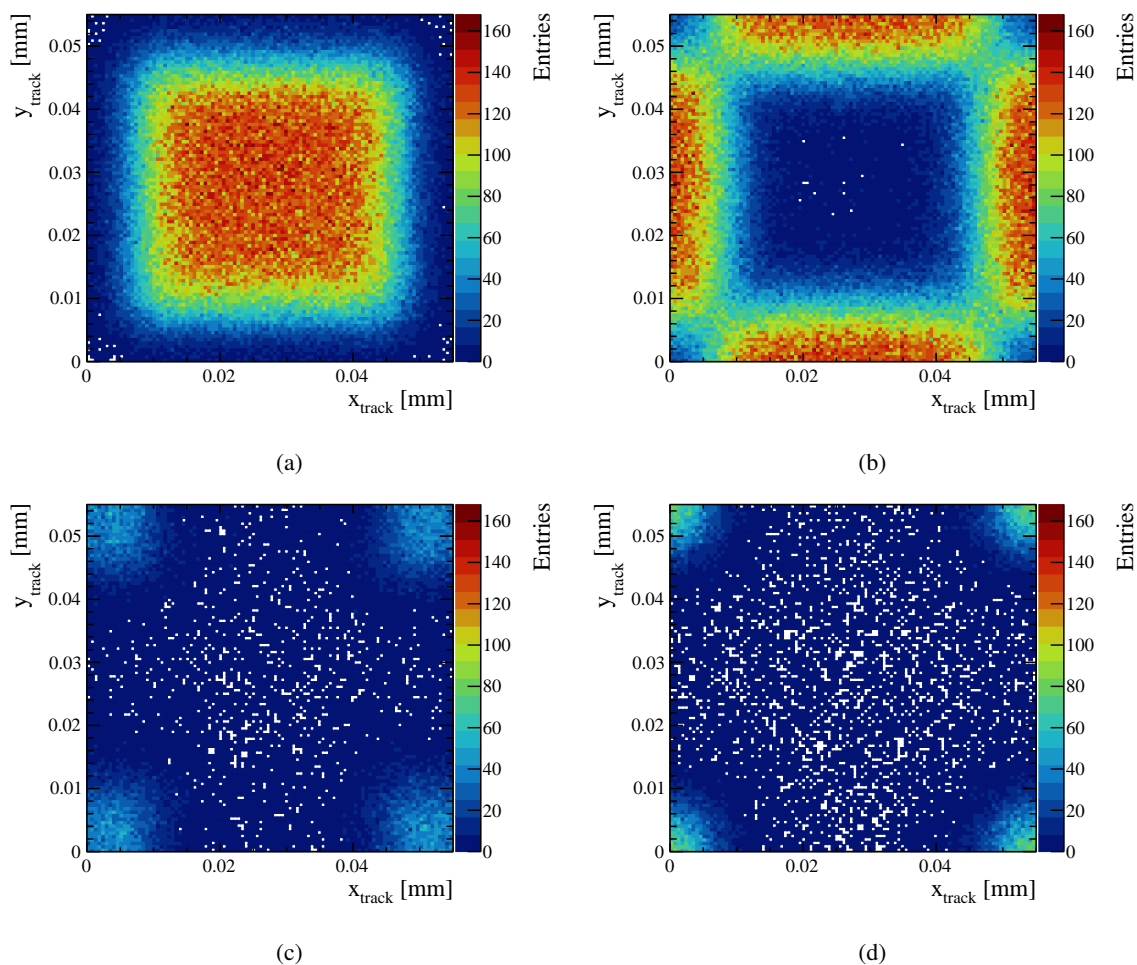
Figure 2. The intrapixel track positions for cluster sizes: size 1 (a), size 2 (b), size 3 (c) and size 4 (d) for an Micron n-on-p sensor (S25).

hence the fraction of size 2 clusters monotonically decreases. Overall, the leakage current increase with bias voltage is very small and is not sufficient to increase the cluster size via noise hits.

For the irradiated prototypes used in this study the bias voltage limit was set at 1000 V, due to unstable operation at higher values and to prevent thermal runaway. For irradiated sensors the measured charge is lower due to the changes in the electric field and charge trapping, the likelihood of shared charge reaching threshold is greatly reduced, affecting cluster sizes and eventually also the efficiency.

In figure 4, the fraction of size 1 and size 2 clusters as a function of applied bias voltage are compared for several prototype sensors placed perpendicular to the beam, uniformly irradiated to the full fluence. At bias voltages below 200 V, the charge is predominantly measured in one pixel. The effect of the irradiation is mitigated by increasing the bias voltage, partially regaining the fraction of size 2 clusters. These effects can be observed in the intrapixel track positions (see appendix C). A minimum in the fraction of size 1 clusters is not observed due to the sensors not being fully depleted at 1000 V [6, 7]. After irradiation, there was no significant increase in noise hits with the threshold set at the default $1000\,e^-$ value. Therefore a noise increase does not affect the cluster size measurements.
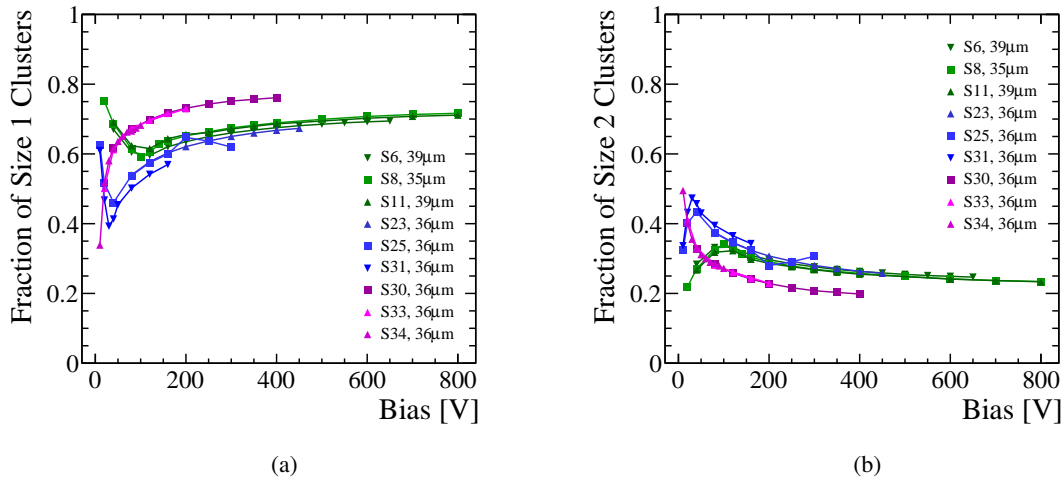
Figure 3. The fraction of size 1 (a) and size 2 (b) clusters as a function of the applied bias voltage. Green for HPK n-on-p, blue for Micron n-on-p and purple for Micron n-on-n.
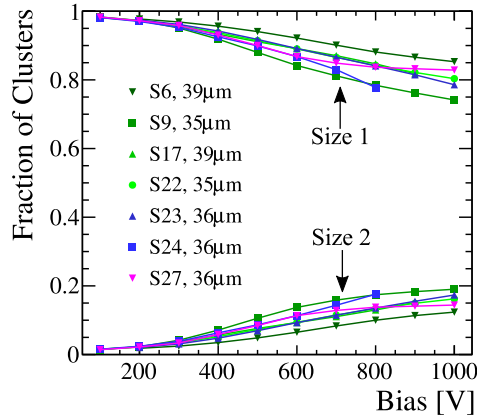

Figure 4. The fraction of size 1 and size 2 clusters for sensors uniformly irradiated to $8 \times 10^{15}\, 1\,\mathrm{MeV}\,\mathrm{n_{eq}\,cm^{-2}}$, placed perpendicular to the beam. Green for HPK n-on-p, blue for Micron n-on-p and purple for Micron n-on-n.

3.2 Track angle

To study the sensor performance for angled tracks, angle scans were performed focusing on the range between approximately 0° and 24°, in order to cover the LHCb acceptance [1]. The fraction of size 1 and size 2 clusters as a function of angle is shown in figure 5. For non-irradiated sensors (a), the largest fraction of size 2 clusters occurs at an angle of around 16° for the Micron n-on-p devices and around 18° for the HPK n-on-p devices, which are roughly compatible with the naive calculation of 15° (section 2.3). The difference between the vendors is consistent with the slight variations in the thickness of the sensors [10]. For the Micron n-on-n devices, 150 μm thick, the largest fraction is expected to be around 20°. However the fraction does not seem to decrease below angles of 24° which is the limit of the scan. After irradiation (figure 5 (b)), the curves show a behaviour similar to that of a thinner sensor, because of the reduced effective depletion depth. The intrapixel track positions depending on cluster size for three different track angles are shown in appendix C
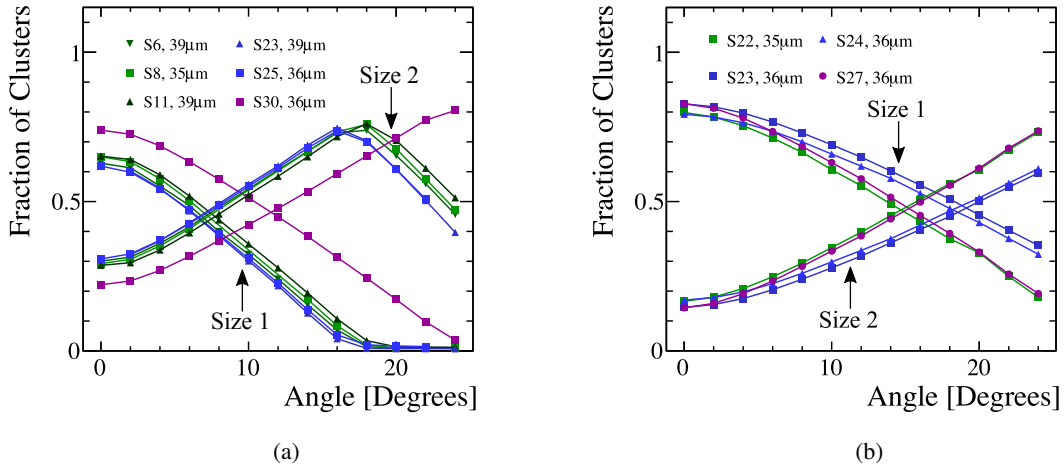
Figure 5. The fraction of size 1 and size 2 clusters as a function of angle, (a) for non-irradiated and (b) for sensors irradiated uniformly to $8 \times 10^{15}\,1\,\mathrm{MeV}\,n_{eq}\,cm^{-2}$. Green for HPK n-on-p, blue for Micron n-on-p and purple for Micron n-on-n.

4 Efficiency results

Non-irradiated sensors are found to be ≥99% efficient when the applied bias voltage is above ~20 V as shown in figure 6 (a) [15]. However the efficiency degrades due to radiation damage. The efficiency as a function of applied bias voltage is shown in figure 6 (b), for several sensors uniformly irradiated to a fluence of $8 \times 10^{15}\,1\,\mathrm{MeV}\,n_{eq}\,cm^{-2}$. The efficiency is reduced to as low as 20% at 100 V, but is recovered up to 99% at bias voltages higher than 900 V due to increased charge collection [7]. The efficiency loss is not uniform over the pixel cell, but higher at the corners, as can be seen in figure 7. After irradiation the charge collection is much lower. For size 3 and size 4 clusters where the charge is divided it becomes less likely that the signal will be sufficient to cross the threshold. Figure 7 compares the intrapixel efficiencies of two uniformly irradiated 200 µm thick HPK sensors with different implant sizes, operated at 300 V. The difference in implant sizes shows that the efficiency degradation in the corner is probably due to the lower electric field. Overall, the sensor with an implant size of 35 µm is 6% less efficient than a sensor with an implant size of 39 µm when operated at 300 V.

5 Spatial resolution results

The spatial resolution depends on operational parameters, such as bias voltage and threshold, as well as the signal-to-noise ratio, the angle of incidence of the particle and the accumulated radiation damage. In this section the spatial resolution is presented as a function of the bias voltage, track angle and fluence.

5.1 Bias voltage

The spatial resolutions are measured for all the prototype variants as a function of different applied bias voltages for both non-irradiated and irradiated sensors. For the non-irradiated sensors, the
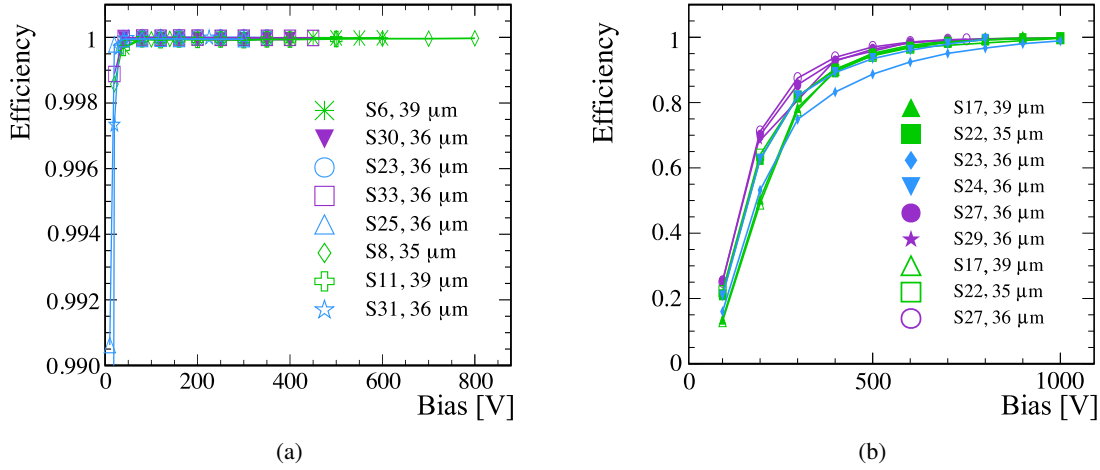
Figure 6. Efficiency as a function of bias voltage, for non-irradiated sensors (a) and irradiated sensors (b). The colour of the markers indicates the vendor and sensor type, where green is for HPK n-on-p, blue is for Micron n-on-p and purple for Micron n-on-n.
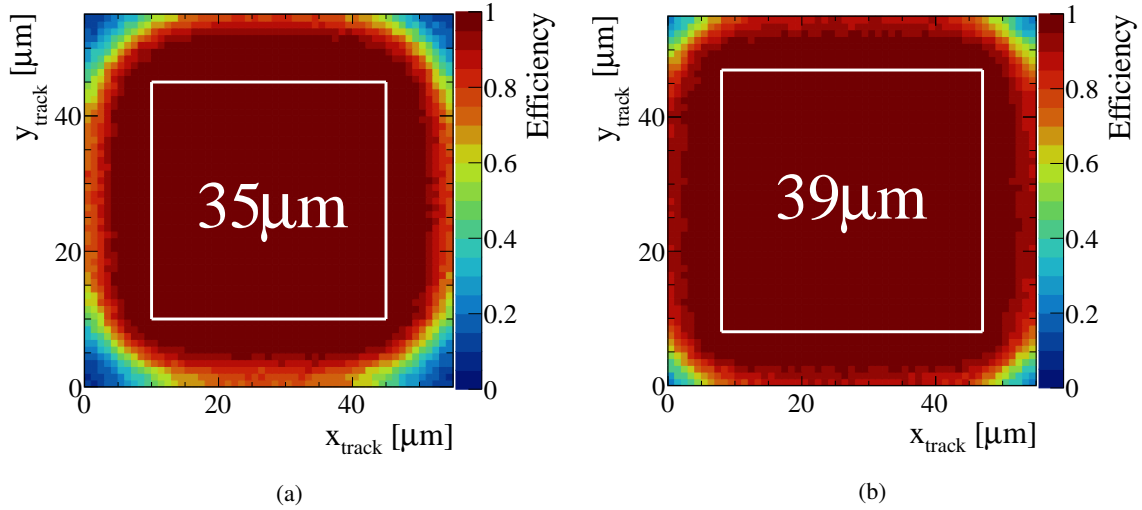

Figure 7. Cluster finding efficiency as a function of the intrapixel position for two 200 μm thick HPK sensors operated at 300 V uniformly irradiated to the full fluence of 8×10^{15} 1 MeV n_{eq} cm^{-2}. The two sensors differ in implant size: S22 has an implant size of 35 μm (a) and S17 has an implant size of 39 μm (b).

resolution in x as a function of the bias voltage is shown in figure 8 (a). The spatial resolution is directly correlated to the cluster size distribution and therefore it follows similar trends as seen in figure 3. For the irradiated sensors, shown in figure 8 (b), the worst resolution is observed between ~300 V and 500 V depending on the sensor. At lower bias voltages, this is due to reduced efficiency especially at the corners, effectively decreasing the pixel area (section 4). Only tracks that pass through the centre of pixel are likely to lead to a measured signal, yielding a smaller residual difference for size 1 clusters thus artificially improving the spatial resolution. At higher bias voltages, the collected charge becomes larger, thereby recovering the efficiency in the corners but also increasing the cluster size. As described in section 3, this improves the resolution.
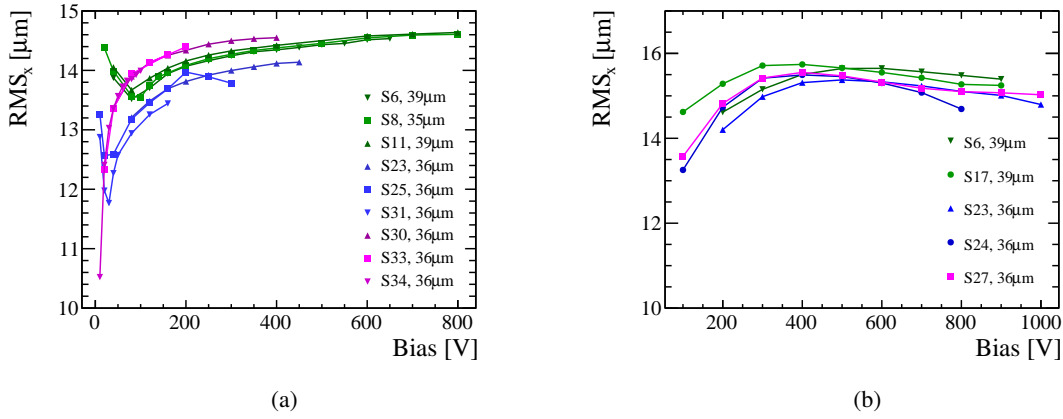
(a)   (b)

Figure 8. The spatial resolution as a function of bias voltage for non-irradiated sensors (a) and for uniformly irradiated sensors to the 8×10^{15} 1 MeV n_{eq} cm^{-2} (b). Green for HPK n-on-p, blue for Micron n-on-p and purple for Micron n-on-n.

5.2 Track angle

The spatial resolution is also measured as a function of the incident track angle. The results for non-irradiated samples are shown in figure 9 (a). All sensors show a similar trend which depends on the thickness, as predicted by eq. (2.3). The optimum resolution is 6.5±0.5 µm at about an angle of 15° and 21°. The quoted uncertainty is from the variation in the measured resolution of the different prototype devices tested of the same type. As described in section 2, the Micron n-on-n prototypes are thinner, and hence the best resolution occurs at a larger angle. After irradiation the active sensor volume is shallower, due to the change in the effective doping concentration [6]. This leads to a less pronounced dependency as a function of the incident angle, even at the highest operational bias voltage, as presented in figure 9 (b). In this plot it can also be seen that the n-on-n prototype behaves quite similar to the thicker sensors, which supports the conclusion that at these fluence levels the sensor thickness is less relevant to the total collected charge.
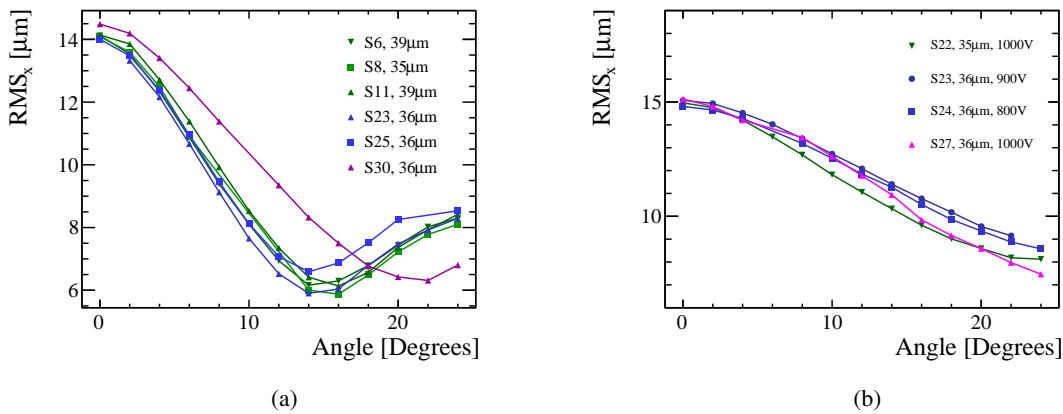

(a)   (b)

Figure 9. The spatial resolution as a function of angle for non-irradiated sensors operated at 200 V (a) and uniformly irradiated sensors to 8×10^{15} 1 MeV n_{eq} cm^{-2} (b). Green for HPK n-on-p, blue for Micron n-on-p and purple for Micron n-on-n.

5.3 Combined bias and track angle

In this section the cross dependence of bias voltage and angle of incidence is discussed. At bias voltages lower than the full depletion, the effective active region of the sensor is thinner. This leads to the effect shown in figure 10, where the spatial resolution is plotted as a function of angle for three different bias voltages for an non-irradiated sensor.
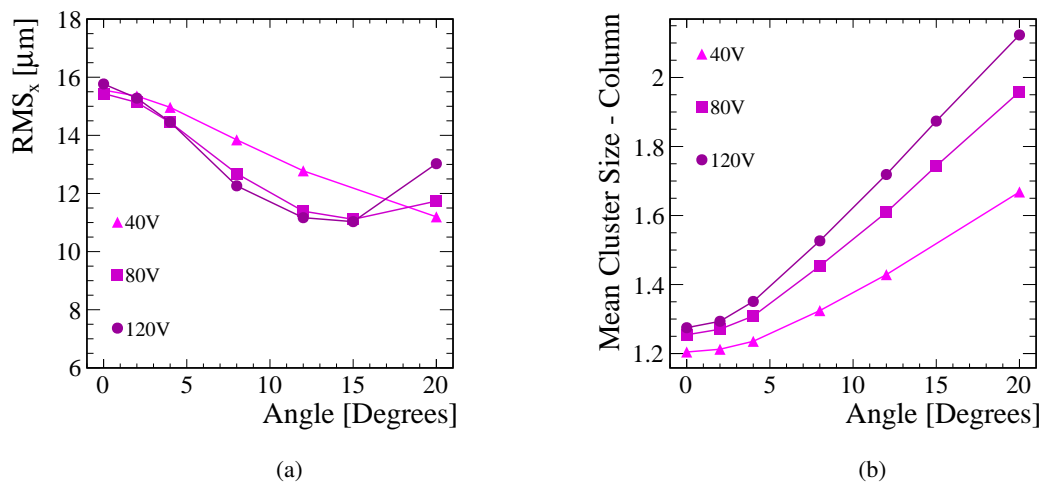

Figure 10. Spatial resolution (a) and the mean cluster size (b) as a function angle, for three different bias voltages for an non-irradiated HPK sensor (S6).

For the irradiated sensors in figure 11 a similar trend is seen, with the caveat that even at the highest voltages the n-on-p sensors are not fully depleted, and only a fraction of the charge is collected. At bias voltages smaller than the maximum operational value the cluster size is smaller since more often a fraction of the shared charge is smaller than the threshold, and the resolution versus angle continues to improve as the applied voltage increases.
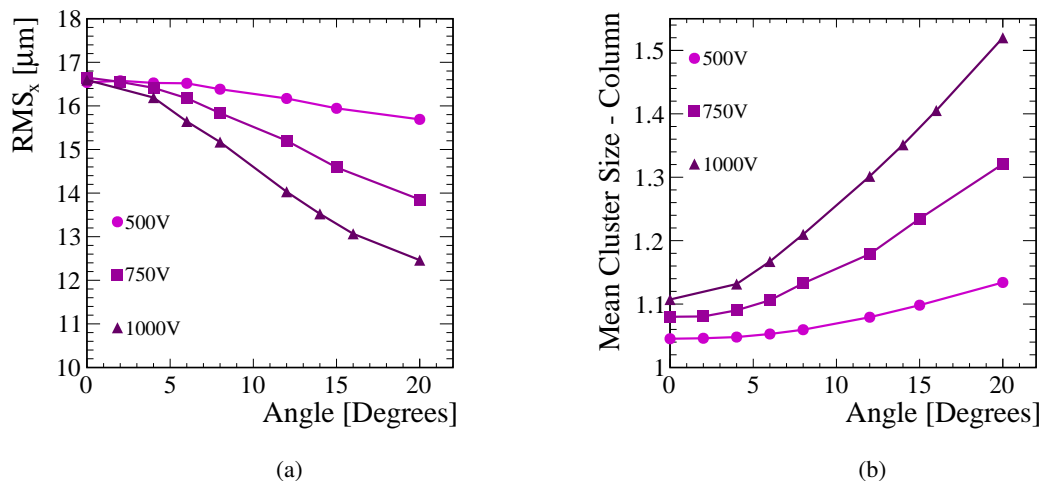

Figure 11. Spatial resolution (a) and the mean cluster size (b) as a function angle, for three different bias voltages for a HPK sensor (S6) uniformly irradiated to the full fluence of 8×10^{15} 1 MeV n_{eq} cm^{-2}.

5.4 Non-uniform irradiation

The spatial resolution and the mean cluster size as a function of the fluence are shown in figure 12 (a) and (b), respectively, for an HPK sensor, placed perpendicular to the beam, operated at 1000 V and non-uniformly irradiated as described in appendix B. For fluences below 4×10^{15} 1 MeV n_{eq} cm^{-2}, the spatial resolution degrades inversely proportional to the fluence. This is because the whole sensor is biased with a single voltage, which means that there are over-depleted regions, precisely where this degradation occurs. At the over-depleted regions the charge sharing decreases as described in section 3, leading to a decrease in cluster size. With increasing fluence, the sensor becomes less over depleted, leading to regions with lower electric and therefore increasing diffusion and consequently more charge sharing. Above 4×10^{15} 1 MeV n_{eq} cm^{-2}, the spatial resolution starts to degrade with increasing fluence and the cluster size decreases due to the irradiation effects, such as charge trapping.
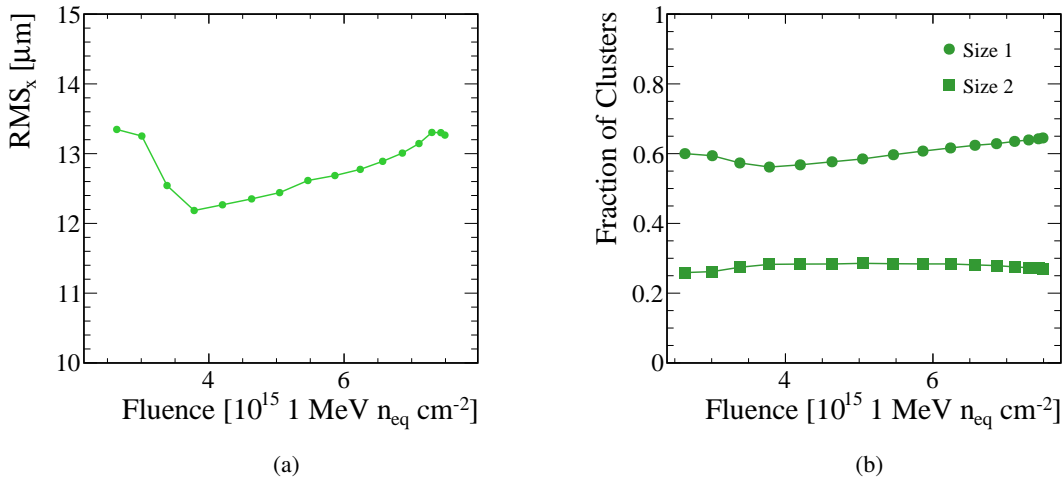

Figure 12. The spatial resolution (a) and the fraction of clusters (b) as a function of fluence, for an HPK sensor operated at 1000 V placed perpendicular to the beam.

6 Conclusions and outlook

In this paper the spatial performance of pixel sensor prototypes bump-bonded to Timepix3 ASICs is presented for sensors before and after irradiation. Irradiated sensors were exposed to either a uniform neutron flux or non-uniform proton irradiation. The maximum fluence was 8×10^{15} 1 MeV n_{eq} cm^{-2} in each case. Sensors were provided by two vendors and the impact of the design differences on the efficiency, cluster size and spatial resolution is assessed.

The non-irradiated sensor measurements indicate a very high efficiency even below full depletion voltage for all prototype variants. The best spatial resolution obtained is 6.5 ± 0.5 μm at about an angle of 15° and 21° for the 200 μm (n-on-p) and 150 μm (n-on-n) thick prototypes, respectively.

For n-on-p sensors, the best resolution for perpendicular tracks is achieved at the depletion voltage. For the n-on-n prototypes, the best resolution is below the depletion since the sensor depletes from the opposite side to the pixel implants, as discussed in section 3.1.

Measurements of the irradiated sensors show a clear decline in efficiency and resolution, which can be mitigated by operating at higher bias voltages. At the fluence of $8 \times 10^{15} \, 1 \, \text{MeV} \, \text{n}_{\text{eq}} \, \text{cm}^{-2}$, which is the expected top value after a total delivered luminosity of $50 \, \text{fb}^{-1}$ at the innermost region of the LHCb VELO detector, all sensor variants remain operational and exceed the minimum efficiency requirement for the LHCb Upgrade. As shown in figure 6, higher efficiencies are obtained for sensors with a larger implant width (39 μm HPK) and at a lower bias voltage values when compared directly to sensors with smaller implant widths (36 μm Micron or 35 μm HPK).

The results presented in this paper validate the sensor candidates as suitable for the application in the LHCb VELO upgrade. Amongst other performance advantages [6, 7], the HPK sensor design with a 39 μm implant width was chosen for the final detector due to its higher efficiency at lower operational bias voltages.

Acknowledgments

A List of assemblies

The details of the sensors that are tested during this analysis are listed here. Two different types of substrates (n-on-p and n-on-n) are used from two different vendors. Further differences between individual assemblies are indicated in the table below.

B Non-uniform irradiation profiles

The IRRAD facility at CERN [9] provides a 24 GeV proton beam that is approximately distributed as a two-dimensional Gaussian, hence yielding a nonuniform fluence profile. After irradiation, the residual activation of the assemblies is obtained by measuring the distribution of hits in the sensor when not exposed to the beam. The hits are caused by the radioactivity induced in the assembly and thus their rate is proportional to the fluence. The radiation profile can then be determined from the activation map, modelled using a two-dimensional Gaussian distribution, further described in ref. [10]. The reconstructed fluence profile of a sensor is shown in figure 13.

Table 2. Table of the prototype sensors tested. For the irradiated profiles the n denotes neutron irradiated and p denotes proton irradiated.

| Sensor	Vendor	Type	Thickness [μm]	Implant [μm]	Guard Ring [μm]	Irradiation Profile	Fluence 1MeVn_{eq}cm^{-2}
S6	HPK	n-on-p	200	39	450	uniform n	8×10^{15}
S8	HPK	n-on-p	200	35	450	non-uniform p	8×10^{15}
S9	HPK	n-on-p	200	35	600	uniform n	8×10^{15}
S11	HPK	n-on-p	200	39	450	non-uniform p	8×10^{15}
S17	HPK	n-on-p	200	39	450	uniform n	8×10^{15}
S22	HPK	n-on-p	200	35	450	uniform n	8×10^{15}
S23	Micron	n-on-p	200	36	450	uniform n	8×10^{15}
S24	Micron	n-on-p	200	36	450	uniform n	8×10^{15}
S25	Micron	n-on-p	200	36	450	non-uniform p	8×10^{15}
S31	Micron	n-on-p	200	35	250	non-irradiated	—
S27	Micron	n-on-n	150	36	450	uniform n	8×10^{15}
S29	Micron	n-on-n	150	36	450	uniform n	—
S30	Micron	n-on-n	150	36	450	non-uniform p	8×10^{15}
S33	Micron	n-on-n	150	36	250	non-irradiated	—
S34	Micron	n-on-n	150	36	250	non-irradiated	—
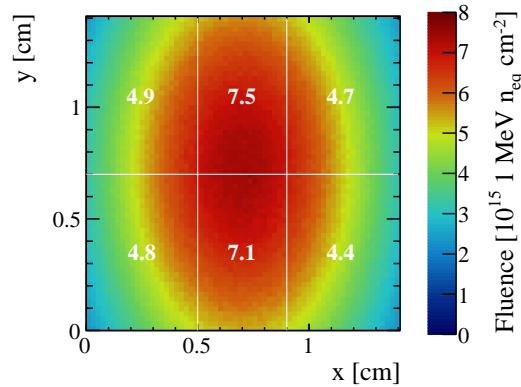
Figure 13. The reconstructed fluence profile from irradiation at IRRAD. The dosimetry results, converted to neutron equivalent fluence, for the six regions are indicated by the white numbers ($\times 10^{15}$ 1 MeV n_{eq} cm^{-2}).

C Intrapixel studies

The intrapixel track positions depending on cluster size 1, 2, 3 & 4 for a Micron n-on-p sensor operated around the depletion voltage and placed perpendicular to the beam was shown previously in figure 2. The same plots are shown in figure 14 for a HPK sensor operated at three different applied

bias voltages (100, 500, 1000 V) for a sensor uniformly irradiated to the 8×10^{15} 1 MeV n_{eq} cm^{-2}. At 100 V, the majority of tracks result in a size 1 cluster due to the inefficiencies described in section 4. At 500 V, the sensor is not yet fully efficient but the number of tracks resulting in size 2 clusters increases. At 1000 V, the sensor is fully efficient.
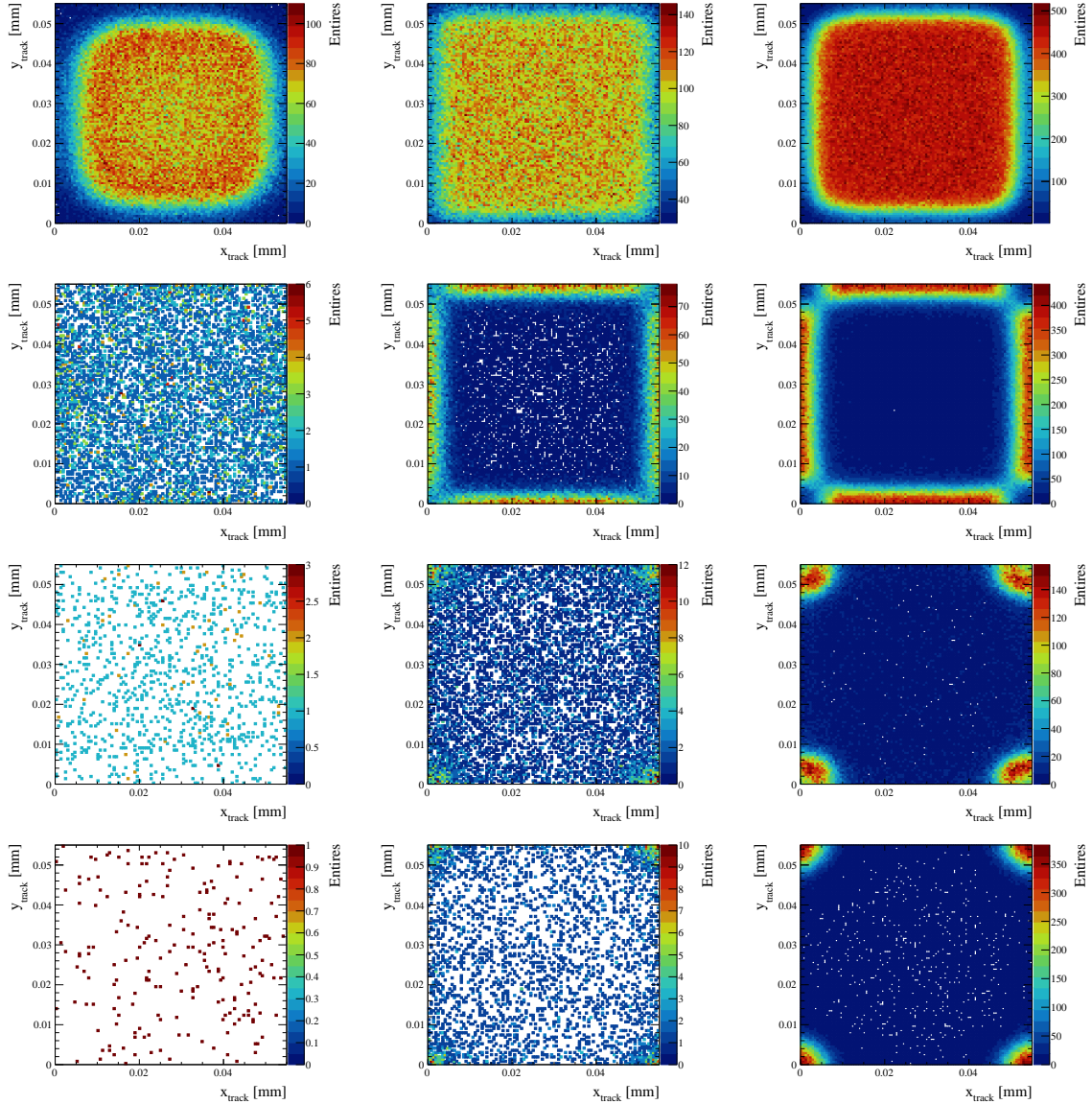

Figure 14. The number of tracks as a function of the intrapixel track positions depending on cluster size for three different applied voltage. The rows are size 1, size 2, size 3 and size 4 from top to bottom and the columns are 100 V, 500 V and 1000 V from left to right. The example shown is for a HPK n-on-p (S9) sensor uniformly irradiated to 8×10^{15} 1 MeV n_{eq} cm^{-2}.

The intrapixel track positions depending on cluster size are also shown in figure 15 for a non-irradiated Micron n-on-p sensor operated around depletion, placed at three different angles (8°, 16° & 22°) relative to the beam. The apparent left-right asymmetry is due to diffusion from the charges moving through longer paths in the sensor.
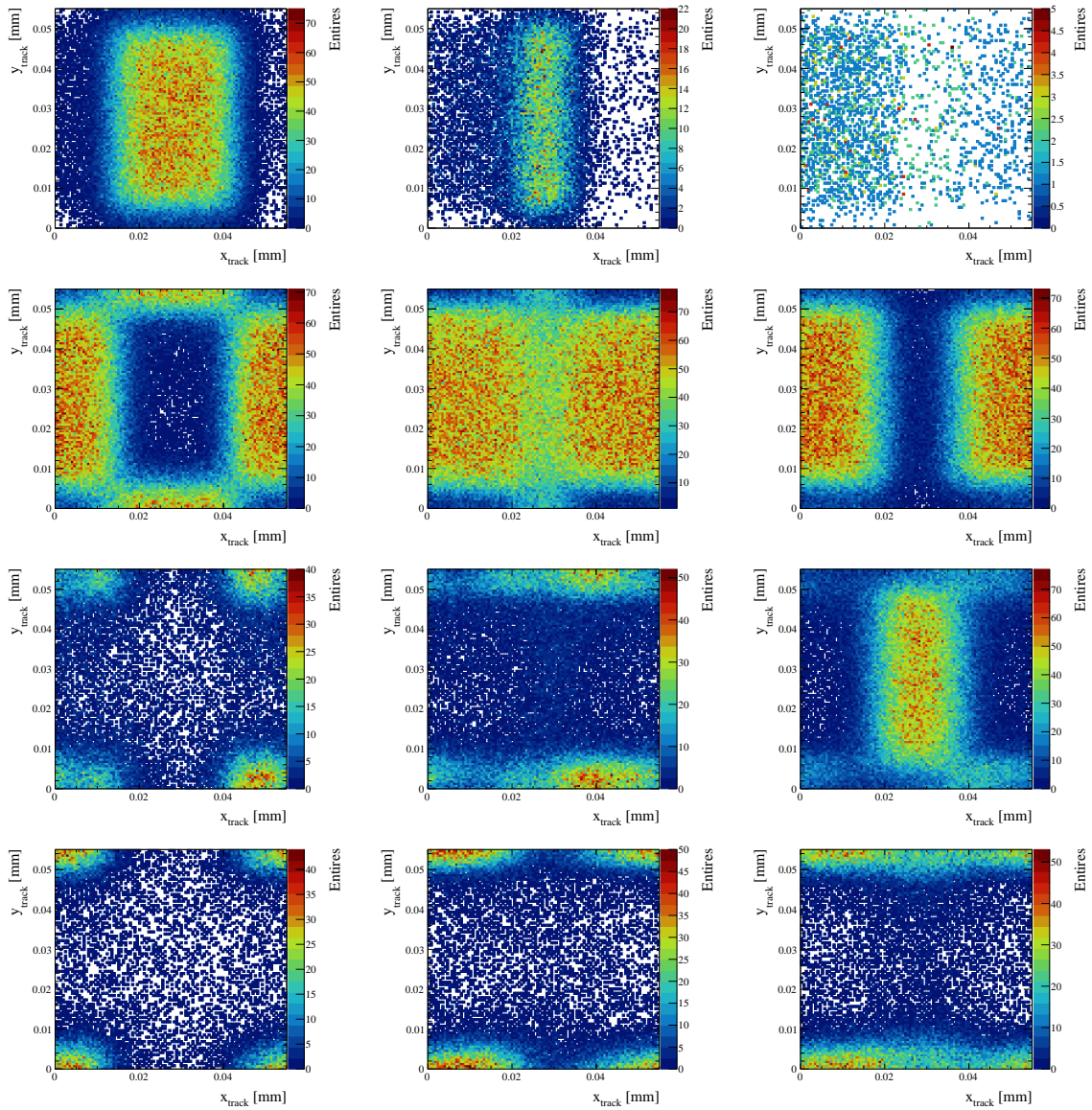
Figure 15. The number of tracks as a function of the intrapixel track positions depending on cluster size for a 200 μm non-irradiated Micron n-on-p sensor (S25) at angles of 8°, 16° and 22° relative to the beam. The rows are size 1, size 2, size 3 and size 4 from top to bottom and the columns are 8°, 16° and 22° from left to right.

References

[1] LHCb collaboration, *LHCb VELO upgrade technical design report*, Tech. Rep. CERN-LHCC-2013-021, CERN, Geneva, Switzerland (2013).

[2] T. Poikela et al., *The VeloPix ASIC*, 2017 *JINST* **12** C01070.

[3] T. Poikela et al., *Timepix3: a 65k channel hybrid pixel readout chip with simultaneous ToA/ToT and sparse readout*, 2014 *JINST* **9** C05013.

[4] K. Akiba et al., *LHCb VELO Timepix3 telescope*, 2019 *JINST* **14** P05026 [`arXiv:1902.09755`].

[5] M. Vicente Barreto Pinto, *Caracterização do TimePix3 e de sensores resistentes à radiação para upgrade do VELO*, master's thesis, Universidade Federal do Rio de Janeiro, Rio de Janeiro, Brazil, February 2016.

[6] E. Dall'Occo et al., *Temporal characterisation of silicon sensors on Timepix3 ASICs*, 2021 *JINST* **16** P07035 [arXiv:2102.06088].

[7] R. Geertsema et al., *Charge collection properties of prototype sensors for the LHCb VELO upgrade*, 2021 *JINST* **16** P02029 [arXiv:2010.10147].

[8] L. Snoj, G. Žerovnik and A. Trkov, *Computational analysis of irradiation facilities at the JSI TRIGA reactor*, *Appl. Radiat. Isot.* **70** (2012) 483.

[9] B. Gkotse, M. Glaser, M. Moll and F. Ravotti, *IRRAD: the new 24 GeV/c proton irradiation facility at CERN*, AIDA-2020-CONF-2016-006, November 2015.

[10] E. Dall'Occo, *Search for heavy neutrinos and characterisation of silicon sensors for the VELO upgrade*, Ph.D. thesis, Vrije Universiteit Amsterdam, Amsterdam, The Netherlands (2020).

[11] CERN, *The Super Proton Synchrotron*, Tech. Rep. https://cds.cern.ch/record/1997188, (2012).

[12] K. Heijhoff et al., *Timing performance of the LHCb VELO Timepix3 telescope*, 2020 *JINST* **15** P09035 [arXiv:2008.04801].

[13] E. Buchanan, *Spatial resolution studies for the LHCb VELO upgrade*, Ph.D. thesis, University of Bristol, Bristol, U.K., October 2018.

[14] H. Spieler, *Semiconductor detector systems*, Oxford University Press, Oxford, U.K. (2005).

[15] S.E. Richards, *Characterisation of silicon detectors for the LHCb vertex locator upgrade*, Ph.D. thesis, University of Bristol, Bristol, U.K., November 2017.